Manuscript (non-LaTeX)

Click here to access/download;Manuscript (non-LaTeX);Manuscript_CAEs-WCEs_revised.pdf

Generation of cold anticyclonic eddies and warm cyclonic eddies in the tropical oceans

Qinbiao Ni[a,b,c], Xiaoming Zhai[b], Zhibin Yang[d] and Dake Chen[a,c]

[a]*State Key Laboratory of Satellite Ocean Environment Dynamics, Second Institute of Oceanography, Ministry of Natural Resources, Hangzhou, China*

[b]*Centre for Ocean and Atmospheric Sciences, School of Environmental Sciences, University of East Anglia, Norwich, UK*

[c]*Southern Marine Science and Engineering Guangdong Laboratory, Zhuhai, China*

[d]*Key Laboratory of Physical Oceanography and Frontiers Science Center for Deep Ocean Multispheres and Earth System, Ocean University of China, Qingdao, China*

Corresponding authors: Qinbiao Ni (niqinbiao@outlook.com) & Zhibin Yang (yang.zhibin@hotmail.com)

ABSTRACT

Mesoscale eddies are ubiquitous features of the global ocean circulation. Traditionally, anticyclonic eddies are thought to be associated with positive temperature anomalies while cyclonic eddies are associated with negative temperature anomalies. However, our recent study found that about one fifth of the eddies identified from global satellite observations are cold-core anticyclonic eddies (CAEs) and warm-core cyclonic eddies (WCEs). Here we show that in the tropical oceans where the probabilities of CAEs and WCEs are high, there are significantly more CAEs and WCEs in summer than in winter. We conduct a suite of idealized numerical model experiments initialized with composite eddy structures obtained from Argo profiles as well as a heat budget analysis. The results highlight the key role of relative wind stress-induced Ekman pumping, surface mixed layer depth and vertical entrainment in the formation and seasonal cycle of these unconventional eddies. The relative wind stress is found to be particularly effective in converting conventional eddies into CAEs or WCEs when the surface mixed layer is shallow. The abundance of CAEs and WCEs in the global ocean calls on further research on this topic.

1. Introduction

Mesoscale eddies, on the order of 100 km and rotating either anticyclonically (AEs) or cyclonically (CEs), are energetic and widespread features throughout the world's oceans (Stammer 1997; Chelton et al. 2007; Ni et al. 2021). These eddies play a vital role in shaping the general ocean circulation, regulating air-sea exchanges, and redistributing climatically important tracers such as heat, salt and carbon (Zhang et al. 2014; Gaube et al. 2015; Conway et al., 2018). Thanks to the availability of global satellite and float observations, significant progress has been made in recent decades on eddy statistics, dynamics and energetics (e.g., Zhai et al. 2010; Chelton et al. 2011; Ni et al. 2020).

Mesoscale AEs (CEs) were traditionally thought to be associated with warm (cold) eddy cores with positive (negative) temperature anomalies that extend from the sea surface to a depth of at least a few hundred of meters (e.g., Roemmich and Gilson 2001; Hausmann and Czaja 2012; Frenger et al. 2013). However, recent studies based on satellite observations (e.g., Everett et al. 2012; Sun et al. 2019; Liu et al. 2020) reported findings of a special subset of oceanic eddies in a number of regions which are characterized by inverse sea surface temperature anomalies (SSTA), that is, cold-core anticyclonic eddies (CAEs) and warm-core cyclonic eddies (WCEs). More recently, using satellite and Argo float data, Ni et al. (2021) suggested that nearly 22% (19%) of the AEs (CEs) detected in the global ocean are CAEs (WCEs) and that the percentages are even higher in the tropical oceans and along the boundary currents. Furthermore, they also found that these unconventional eddies play a distinct role in air-sea momentum and heat exchange, mixed layer dynamics and primary productivity. Similar abundance of CAEs and WCEs in the global ocean was also reported by Liu et al. (2021) who applied deep learning technique to the satellite sea surface height and temperature data.

The afore-mentioned studies demonstrate that CAEs and WCEs are widespread in the global ocean, rather than a feature of curiosity as thought before. There are a few candidate processes that may be responsible for the generation of CAEs and WCEs, for example, boundary flow instability (Chaigneau et al. 2011), exchange of waters inside and outside eddies (Itoh and Yasuda 2010; Sun et al. 2022), barrier layer thickening (He et al. 2020), wind-eddy interaction (McGillicuddy 2015) and eddy-modulated mixing (Moschos et al. 2022). However, none of the above processes have been shown to be the dominant generation mechanism for CAEs and WCEs found in the global ocean. Ni et al. (2021) hypothesized that the depth of surface mixed layer and Ekman pumping due to wind-eddy interaction may be important for the large-scale distribution and seasonal cycle of CAEs and WCEs in the open ocean. Specifically, they argued that Ekman pumping associated with wind-eddy interaction (Gaube et al. 2015; McGillicuddy 2015) acts to raise and depress the near-surface isotherms in AEs and CEs respectively which may reverse the sign of near-surface temperature anomalies in these eddies, especially when the surface mixed layer is shallow. Here, we investigate the generation of CAEs and WCEs in the tropical regions using a combination of observational analysis and numerical modeling, with a particular focus on the role of wind-eddy interaction and mixed layer depth.

The present paper is organized as follows. The observed seasonal cycles of CAEs and WCEs, surface wind speed and mixed layer depth in the tropical oceans are described in section 2. The vertical structures of mesoscale eddies are composited and reconstructed using Argo float profiles in section 3. In section 4 we explain the configuration of an idealized model used to investigate the mechanism of the observed CAEs and WCEs and in section 5 we perform the numerical experiments and conduct a heat budget analysis to diagnose the key processes for generating CAEs and WCEs. Finally, conclusions are given in section 6.

2. Observed seasonal variations

In this study, the global sea level anomaly (SLA) data during the period from 1998 to 2017 were obtained from the Copernicus Marine Environment Monitoring Service (http://marine.copernicus.eu/), which merge the TOPEX/Poseidon, Jason-1, ERS-1/2 and Envisat altimetry records. The global microwave sea surface temperature (SST) data for the same 20-yr period were obtained from the Remote Sensing Systems (http://www.remss.com/). Both datasets are provided with a temporal resolution of 1 day and a spatial resolution of 1/4°. Before conducting the analysis of mesoscale eddies, each SLA and SST map was high-pass-filtered using a spatial Gaussian filter with a half-power cutoff wavelength of 10° to remove large-scale signals related to wind forcing and surface heating/cooling (Ni et al. 2021). The eddy identification method applied here is based on the SLA geometry (Chelton et al. 2011; Chaigneau et al. 2011), the eddy tracking method is based on the dissimilarity parameter (Penven et al. 2005; Souza et al. 2011) and the eddy classification method is based on the signs of SLA and SSTA (Assassi et al. 2016; Ni et al. 2021). An eddy is regarded as a CAE or WCE if the SLA and SSTA at the eddy center are of opposite signs; Otherwise, it is regarded as a conventional eddy. Readers are referred to Ni et al. (2020; 2021) for detailed descriptions of the eddy detection, tracking and classification methods. Globally, about 9.4 (9.6) million snapshots of 127,42 (133,780) anticyclonic (cyclonic) eddies with lifetime longer than 4 weeks were identified over the 20-yr study period, among which approximately one-fifth was classified as CAEs and WCEs (Ni et al. 2021).

The proportions of CAEs and WCEs are noticeably higher in the tropical regions, forming a zonal belt of high probability of occurrence on either side of the Equator (Fig. 1). To shed light on the key factors responsible for these tropical belts of CAEs and WCEs, we first examine the observed seasonal variations of these eddies in the low latitude band from 5° to 25° in both hemispheres. Regardless of the hemisphere, both CAEs and WCEs are found to occur more frequently during summer than during winter (Figs. 2a and c). Similar seasonal variations in the occurrence of CAEs and WCEs have also been found at mid latitudes of the Northern Pacific Ocean (Ni et al. 2021). In addition, the proportion of CAEs is found to be consistently higher than that of WCEs throughout the year. This systematic difference is likely related to the generation mechanism of these unconventional eddies, which we will explore later in our numerical experiments.

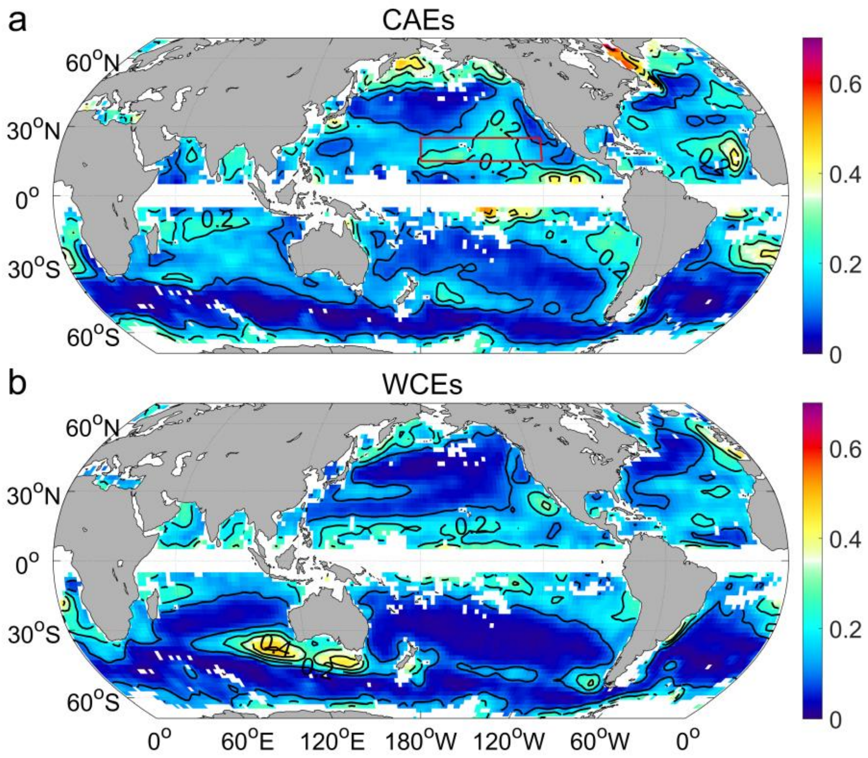

FIG. 1. The proportions of the number of snapshots of (a) cold-core anticyclonic eddies (CAEs) and (b) warm-core cyclonic eddies (WCEs) to the total number of snapshots of eddies detected in global 2°×2° bins during the period from 1998 to 2017 (from Ni et al. 2021).

Next, we examine the observed seasonal cycle of the surface wind speed and mixed layer depth in the tropical regions, two factors hypothesized to be important for the generation of CAEs and WCEs (Ni et al. 2021). The daily 0.25°×0.25° QuikSCAT scatterometer wind speed data provided by the French Research Institute for Exploitation of the Sea (http://cersat.ifremer.fr/) from 2000 to 2009 are used here. The mixed layer depth is defined as the depth where the temperature differs by 0.2°C (de Boyer Montégut et al. 2004) from the temperature at 10-m depth in Argo float profiles. The Argo profile data are obtained from the China Argo Real-time Data Center (http://www.argo.org.cn/) for the same period as the SLA data. Our results show that the surface wind speed averaged over the tropical ocean latitude band remains relatively constant throughout the year, with a mean magnitude of around 6.75 m s^{-1} (Figs. 2b and d). In contrast, the mixed layer depth exhibits a marked seasonal cycle. The mixed layer depth averaged over the low latitude bands increases from about 40 m in summer to about 65 m (80 m) in winter in the Northern (Southern) Hemisphere. The inverse relationship between the seasonal cycle of mixed layer depth and that of CAE and WCE percentages suggests that the surface mixed layer may play an important role in the formation of CAEs and WCEs in the tropical regions.

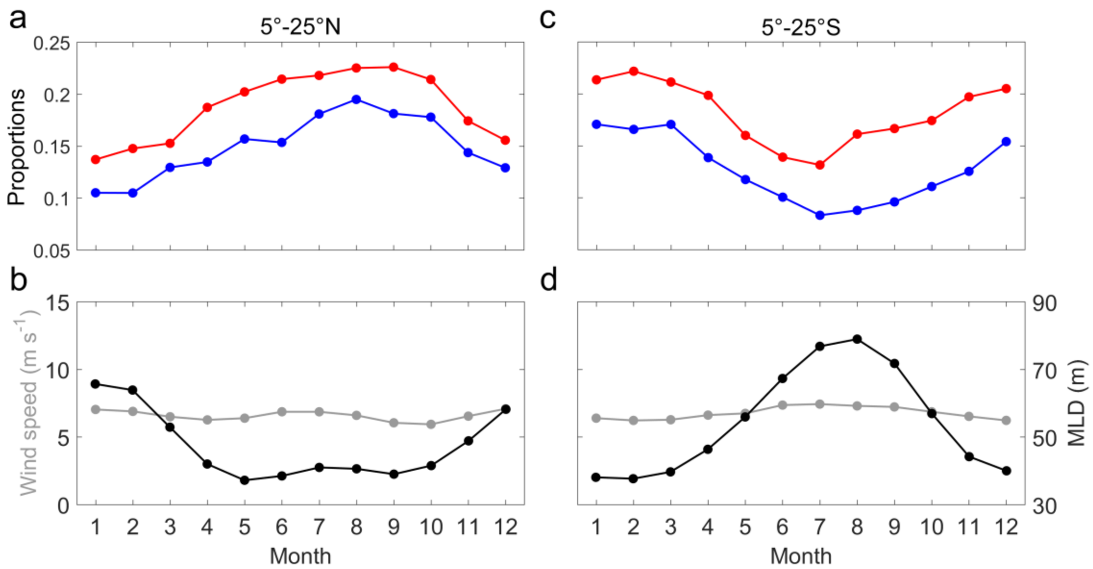

FIG. 2. Seasonal cycles of the proportions of (a) the CAEs (red) and WCEs (blue) and (b) the wind speed (grey; m s^{-1}) and mixed layer depth (black; m) averaged in the low latitude band of the Northern Hemisphere (5°-25°N). (c, d) As Figs. 2a, b but averaged in the low latitude band of the Southern Hemisphere (5°-25°S).

3. Eddy structure

To characterize typical vertical eddy structures in the tropical oceans, here we make use of 25,149 quality-controlled Argo float profiles located in the red box in Fig. 1a. Only Argo profiles with temperature and salinity measurements available at depths from 10 m to 1800 m are selected. The temperature (T') and salinity (S') anomalies of an Argo profile are obtained by subtracting a local climatological profile from the temperature (T) and salinity (S) measurements. This climatological profile is produced by averaging all the Argo profiles inside an area of 5°×5° and within 45 days centered at the profile under consideration. Using these Argo profiles, we composite the eddy T' and S' after objectively interpolating them onto an eddy-centric coordinate system (Ni et al. 2021). Note that the sign of Argo profiles associated with CEs is reversed before the composite analysis procedure. Figures 3a and b show the composite vertical eddy T' and S' profiles (solid curves) at the center of the conventional eddies, respectively. For comparison, we also plot the composite eddy T' profile at the center of the unconventional eddies (dashed curve in Fig. 3a). It is found that T' associated with the CAEs and WCEs has an opposite sign to that associated with the conventional eddies in the upper ~30 m or so.

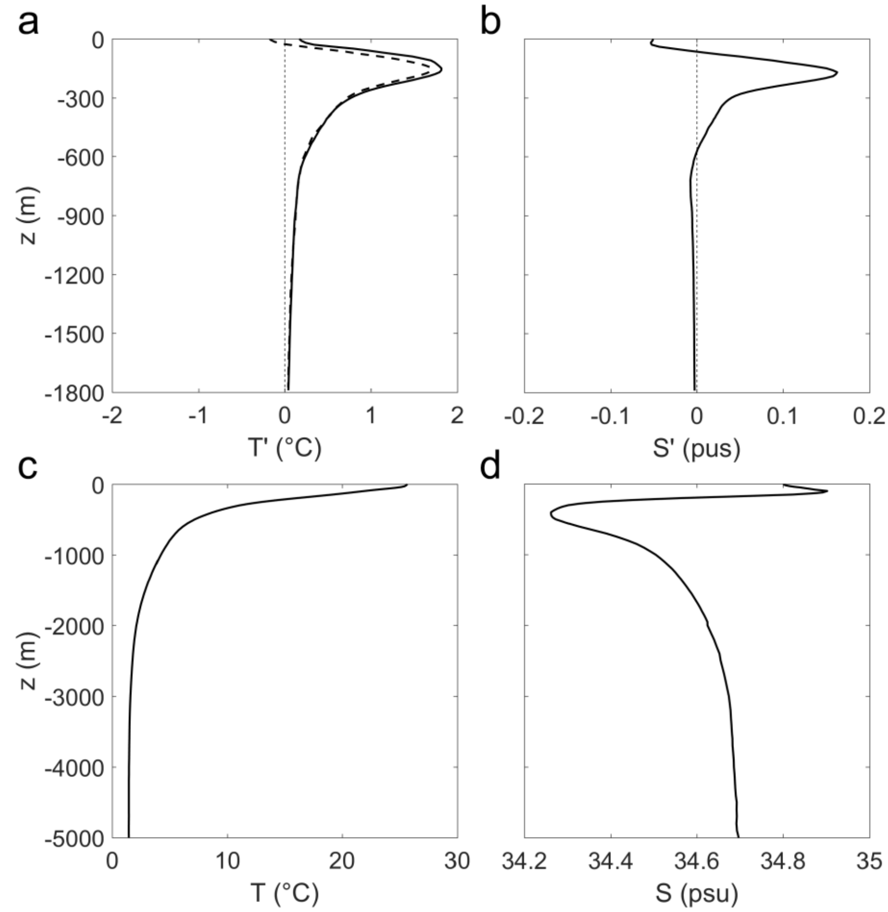

FIG. 3. (a, b) Vertical profiles of temperature anomaly (T'; °C) and salinity anomaly (S'; psu) at the center of the composite conventional (solid curves) and unconventional (dashed curve) eddies based on Argo float data in the region (180°-240°E, 15°-25°N) marked by the red box in Fig. 1a. Note that the sign of the Argo profiles associated with cyclonic eddies (CEs) is reversed before the composite analysis procedure. (c, d)

Vertical temperature (T; °C) and salinity (S; psu) profiles of WOA18 climatological data averaged in the same region.

We then combine the vertical eddy T' profile (T_v') at the center of the composite eddy with a horizontal Gaussian function (G_h; McGillicuddy 2015) to reconstruct the 3D T' structures of an idealized AE and an idealized CE via $T' = \pm T_v' \cdot G_h$. Since the composite T' represents eddy temperature anomalies averaged over different stages of eddy lifetime which already include imprints of various damping effects such as wind-eddy interaction (Xu et al. 2016; Rai et al. 2019), we augment the magnitude of T' by a factor of 1.5 before it is used further to construct the initial eddy conditions for the numerical simulations. The 3D structure of eddy S' is constructed in the same way. These eddy-induced T' and S' anomalies are then added to the climatological-mean temperature and salinity profiles of the World Ocean Atlas 2018 (WOA18) data (Figs. 3c and d) averaged horizontally over the same red box in Fig. 1a to provide the full-depth initial 3D eddy temperature and salinity fields for use in our idealized model experiments. Figure 4 shows that the initial AE (CE) temperature field is axis-symmetric, characterized by positive (negative) SSTA and depressed (raised) isothermal surfaces inside the eddy. The initial eddy horizontal velocities are derived from the eddy temperature and salinity fields via the thermal wind balance.

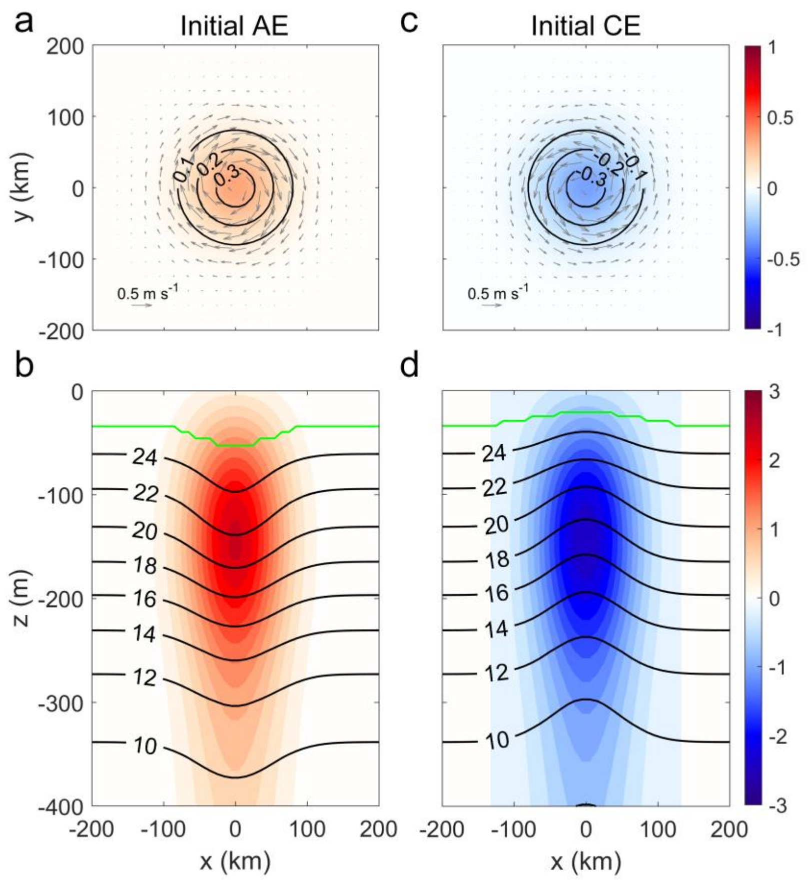

FIG. 4. Initial eddy temperature and temperature anomaly fields used in the numerical experiments. (a) Sea surface temperature anomaly (SSTA; °C) of an anticyclonic eddy (AE). Gray arrows indicate eddy surface geostrophic currents calculated from the sea surface height. (b) Vertical T (contours; °C) and T' (colors; °C) structures of the AE across y = 0. The mixed layer depth (MLD) is marked by the green curve. (c, d) As Fig. 4a, b but for a cyclonic eddy (CE).

4. Model configuration

To further investigate the role of wind-eddy interaction in the generation of CAEs and WCEs in the tropical regions, we conduct a suite of idealized numerical experiments using the Massachusetts Institute of Technology General Circulation Model (MITgcm; Marshall et al. 1997). The model has a box-like domain that is 700 km long, 700 km wide and 4266 m deep, with double periodic boundary conditions. The horizontal resolution of the model is a uniform 10 km. A variable vertical resolution is used ranging from 1 m near the surface to 250 m near the bottom (83 levels in total), following the configuration of the Estimating the Circulatioan and Climate of the Ocean, phase 2 (ECCO2). The initial eddy has a radius of 100 km and is located at the center of the model domain. To avoid the complication of eddy propagation and dispersion, the model sits on an f plane at a latitude of 20°N. The horizontal mixing employs a Laplacian operator with a coefficient of 5 m^2 s^{-1} and the vertical mixing adopts the K-profile parameterization scheme (Large et al. 1994) with a background diffusivity of 10^{-5} m^2 s^{-1}.

Two types of wind stress are used in the numerical simulations: absolute wind stress $\tau_{abs} = \rho_{air} c_d \boldsymbol{u}_{air} |\boldsymbol{u}_{air}|$ and relative wind stress $\tau_{rel} = \rho_{air} c_d (\boldsymbol{u}_{air} - \boldsymbol{u}_{sea}) |\boldsymbol{u}_{air} - \boldsymbol{u}_{sea}|$, where ρ_{air} is the air density, c_d is the drag coefficient which is calculated online in the EXF package of MITgcm, $\boldsymbol{u}_{air}$ is the surface wind velocity and $\boldsymbol{u}_{sea}$ is the surface ocean current velocity. The absolute wind stress depends on surface winds alone, whereas the relative wind stress accounts for the relative motion between the surface winds and surface ocean currents. It is well known that the interaction between relative wind stress and ocean eddies leads to Ekman upwelling (downwelling) inside AEs (CEs) which acts to raise (depress) the upper ocean density surfaces of AEs (CEs) (Gaube et al. 2015; McGillicuddy 2015; Wilder et al. 2022), while no such Ekman pumping motion is induced by absolute wind stress (Fig. A1). Therefore, comparison between relative and absolute wind stress experiments can be used to highlight the role of relative wind stress-eddy interaction in the generation of CAEs and WCEs in the tropical regions. Here we use a spatially uniform wind speed with a magnitude of 6.75 m s^{-1} as this is the average wind speed observed in the tropical regions (Fig. 2). Following McGillicuddy (2015), the wind direction rotates anticlockwise with a period of ~3 days which is about twice longer than the local inertial period. The reason for rotating wind direction is to maintain the symmetry of the simulated eddies by minimizing Ekman transport and choosing a 3-day rotation period avoids resonant excitation of significant inertial motions in the model experiments.

The surface mixed layer depth has been hypothesized to be an important factor in the formation of CAEs and WCEs (Ni et al. 2021). The mixed layer depth is strongly influenced by both surface heat flux and wind stress (McGillicuddy 2015). While the wind stress acts to mix the upper ocean all year round, surface heat fluxes stratify the upper ocean via solar heating in summer and deepen the surface mixed layer via cooling-induced convective mixing in winter. As a result, the surface mixed layer depth in the tropical regions exhibits pronounced seasonal variations as shown in Fig. 2. Here we use surface heat flux forcing as a means of controlling the mixed layer depth in our model experiments to represent summer and winter conditions. For both the initial AE and CE, we conduct four numerical experiments. In the first three experiments, the AE or CE is subject to the relative wind stress together with surface heat fluxes with a magnitude of 50, 20 and -50 W m^{-2}, respectively. The fourth experiment is forced by the absolute wind stress and surface heat flux of 50 W m^{-2} (Table 1). Note that the surface heat fluxes are spatially uniform in the model domain of all the experiments.

TABLE 1. Idealized numerical experiments

Experiment	Eddy polarity	Wind stress	Surface heat flux (W m^{-2})
Q+50AE_rel	Anticyclonic	$\tau = \rho_{air} c_d (\boldsymbol{u}_{air} - \boldsymbol{u}_{sea}) \lvert \boldsymbol{u}_{air} - \boldsymbol{u}_{sea} \rvert$	50
Q+50CE_rel	Cyclonic		50
Q+20AE_rel	Anticyclonic		20
Q+20CE_rel	Cyclonic		20
Q-50AE_rel	Anticyclonic		-50
Q-50CE_rel	Cyclonic		-50
Q+50AE_abs	Anticyclonic	$\tau = \rho_{air} c_d \boldsymbol{u}_{air} \lvert \boldsymbol{u}_{air} \rvert$	50
Q+50CE_abs	Cyclonic		50

5. Results

5.1 Generation mechanism

We start with experiments Q+50AE_rel and Q+50CE_rel, which are forced by relative wind stress and surface heat flux of 50 W m^{-2}. These experiments are designed to simulate the evolution of AE and CE under relative wind stress forcing in summer, respectively. In both experiments, the surface mixed layer is maintained at about 20 m by the combined effect of wind stress-induced mixing and surface heating, albeit the stratification at the base of the mixed layer continues to increase due to positive surface heat flux (Figs. 5a-c and 6a-c).

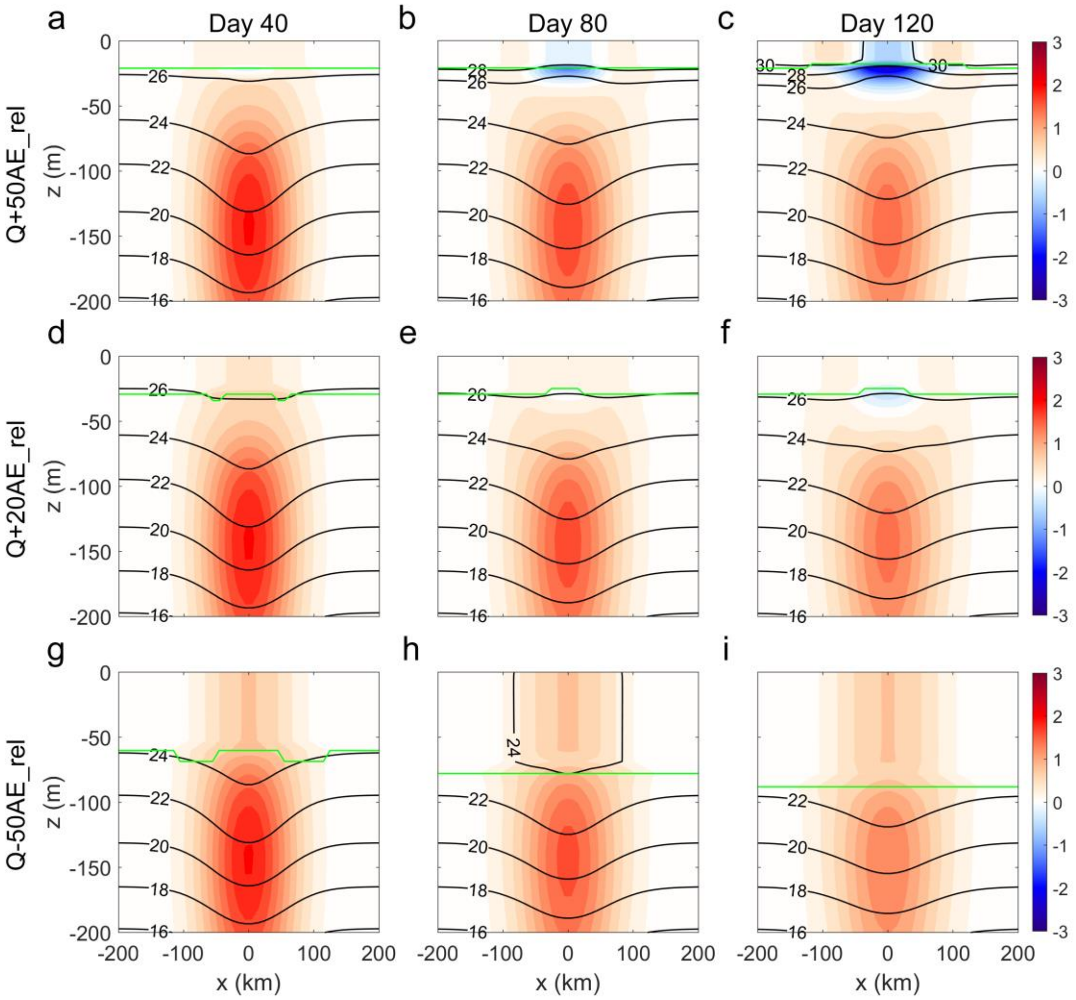

FIG. 5. Vertical structures of temperature (contours; °C) and temperature anomalies (colors; °C) at y=0 (see Fig. 4a) in the AE experiments on day 40, 80 and 120 under relative wind stress and with surface heat flux of (a-c) 50 W m^{-2}, (d-f) 20 W m^{-2} and (g-i) -50 W m^{-2}. The green curves indicate the MLDs.

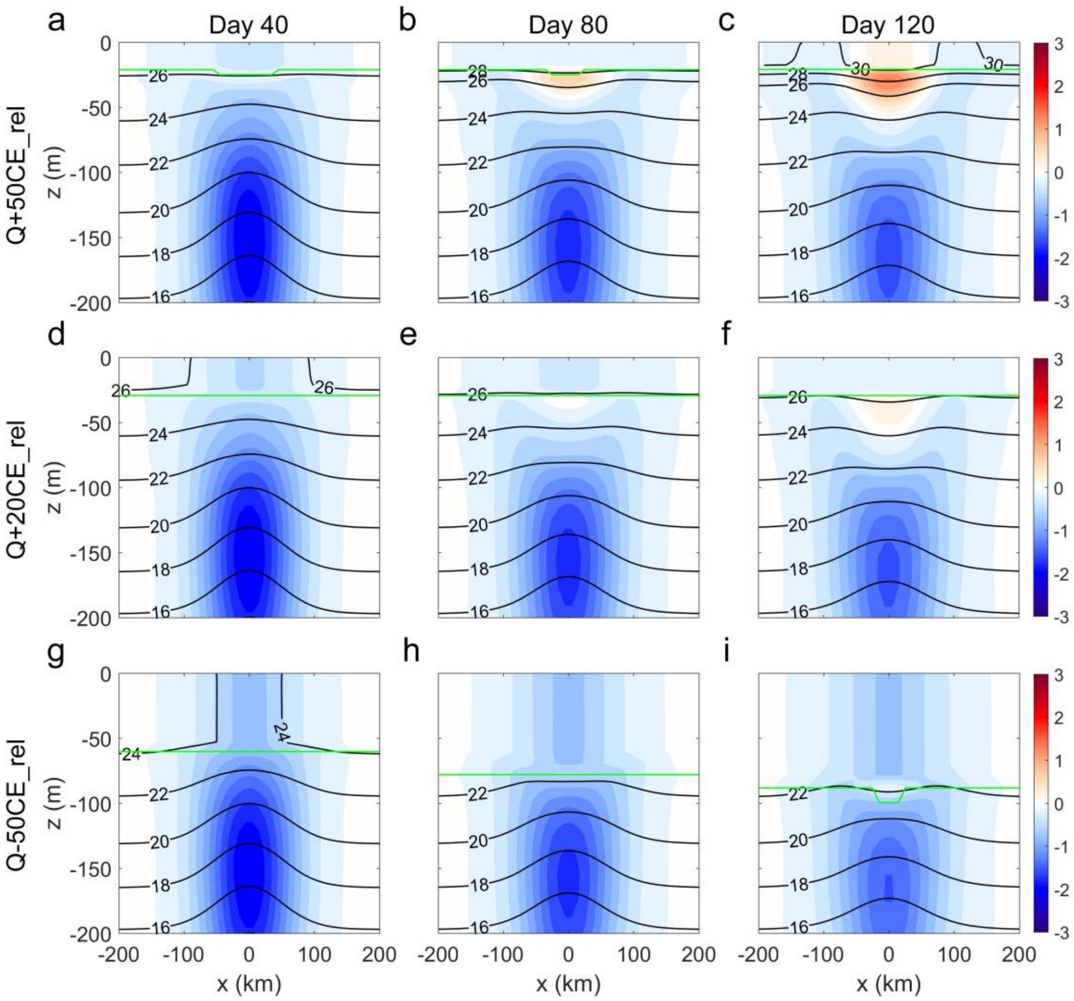

FIG. 6. As Fig. 5 but for the CE experiments.

Ekman divergence and upwelling induced by relative wind stress inside the AE is seen to gradually raise the depressed isotherms of the AE throughout the water column. As a result, the maximum temperature anomaly at ~150 m associated with the AE decreases from the initial 3°C to ~1°C on day 120. Note that temperature anomalies here refer to deviations from the background temperature, i.e., temperature away from the eddy at the edge of the model domain, rather than deviations from the initial condition. At the base of the shallow mixed layer in these two experiments where the Ekman pumping velocity is large and the initial positive temperature anomaly of the AE is relatively small, Ekman pumping is able to raise the isotherms of the AE and reverse the sign of temperature anomalies to negative at the base of the mixed layer (Fig. 5b). As vertical mixing mixes the surface water with the water below, these negative temperature anomalies at the base of the mixed layer are entrained into the mixed layer, generating negative SSTA (Fig. 7b). In this way, the initial AE evolves into a CAE. With further action of Ekman upwelling, the negative temperature anomalies at the base of the mixed layer intensify as well as expand in the vertical direction (Fig. 5c). On day 120, the negative SSTA at the center of the CAE reaches a magnitude of -0.4ºC (Fig. 7c).

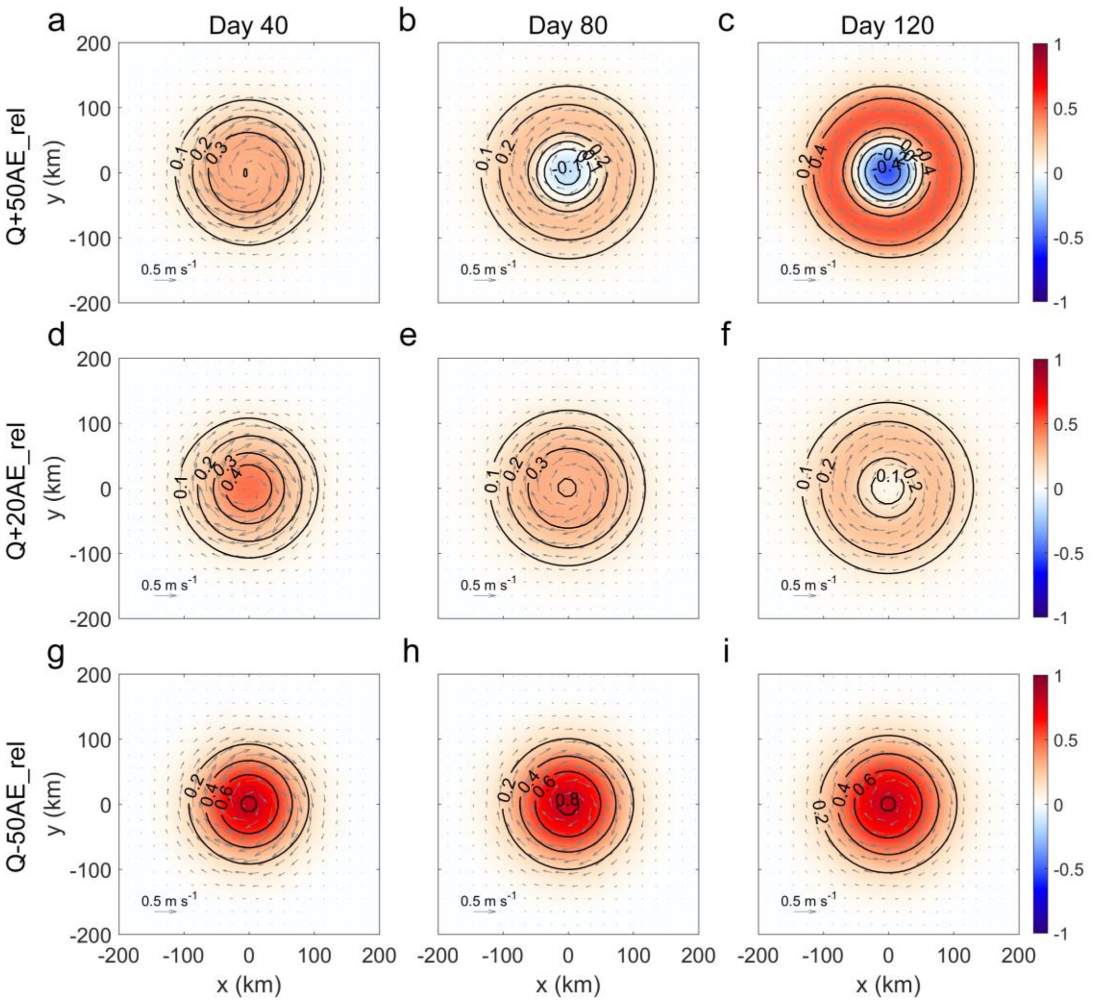

FIG. 7. SSTA (°C) patterns in the AE experiments on day 40, 80 and 120 under relative wind stress and with surface heat flux of (a-c) 50 W m^{-2}, (d-f) 20 W m^{-2} and (g-i) -50 W m^{-2}. The arrows indicate surface eddy geostrophic currents derived from sea surface height.

Similarly, Ekman convergence and downwelling induced by relative wind stress inside the CE lowers the initially raised isotherms of the CE and build up positive temperature anomalies near the base of the mixed layer (Fig. 6b). Surface turbulent mixing, in turn, entrains waters with these positive temperature anomalies and mix them with the surface water to produce positive SSTA (Fig. 8b). In this way, a WCE is generated. On day 120, the magnitude of positive SSTA at the center of the WCE increases to 0.2ºC (Fig. 8c) which is about half of the magnitude of negative SSTA of the CAE.

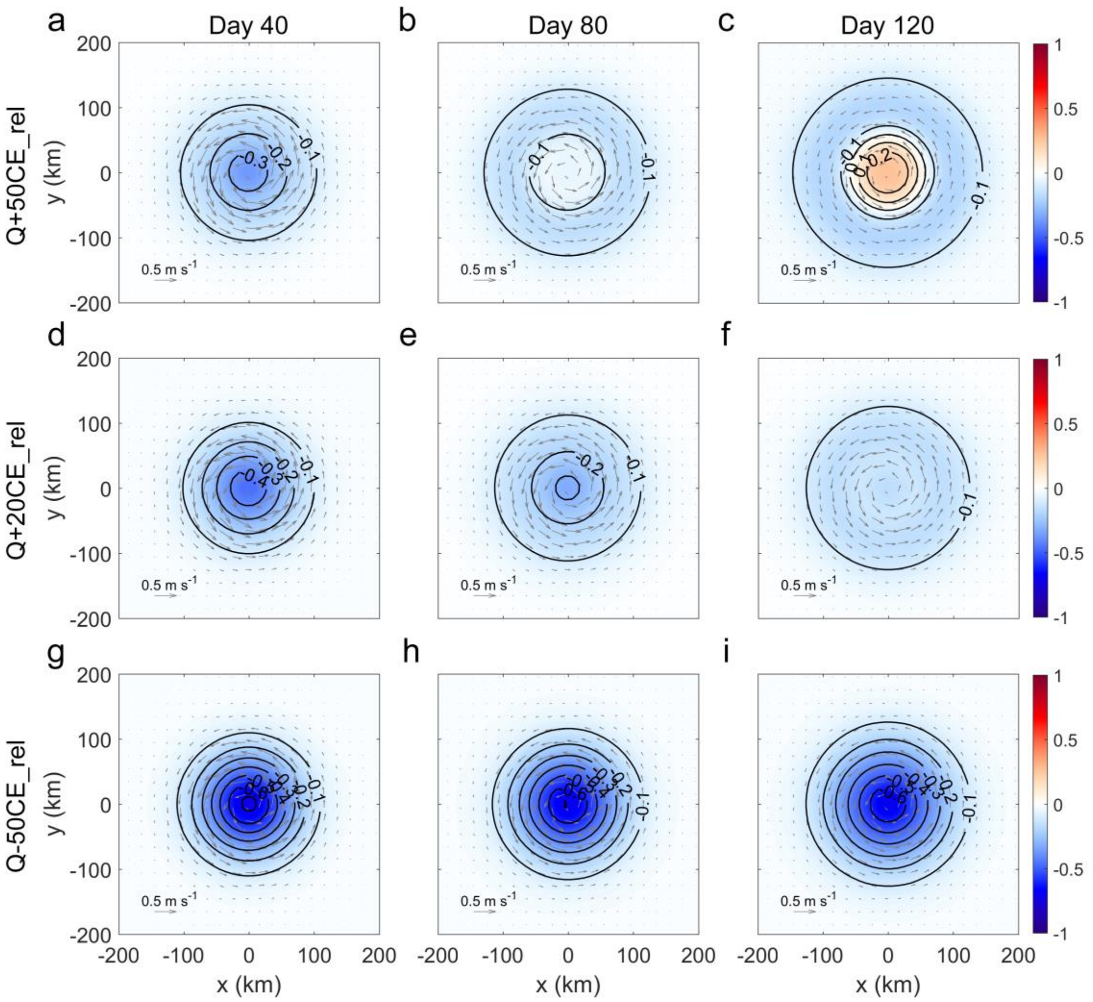

FIG. 8. As Fig. 7 but for the CE experiments.

A different picture emerges if the same AE and CE are subject to absolute wind stress. Experiments Q+50AE_abs and Q+50CE_abs are the same as Q+50AE_rel and Q+50CE_rel except that the relative wind stress is replaced by the absolute wind stress. In the absence of Ekman pumping induced by relative wind stress, the AE and CE are only slightly attenuated in the two absolute wind stress experiments (Fig. 9). There are no negative (positive) temperature anomalies built up at the base of the mixed layer and no development of negative (positive) eddy SSTA in Q+50AE_abs (Q+50CE_abs). Comparison between the relative and absolute wind stress experiments highlights the central role of relative wind stress in the generation of CAEs and WCEs.

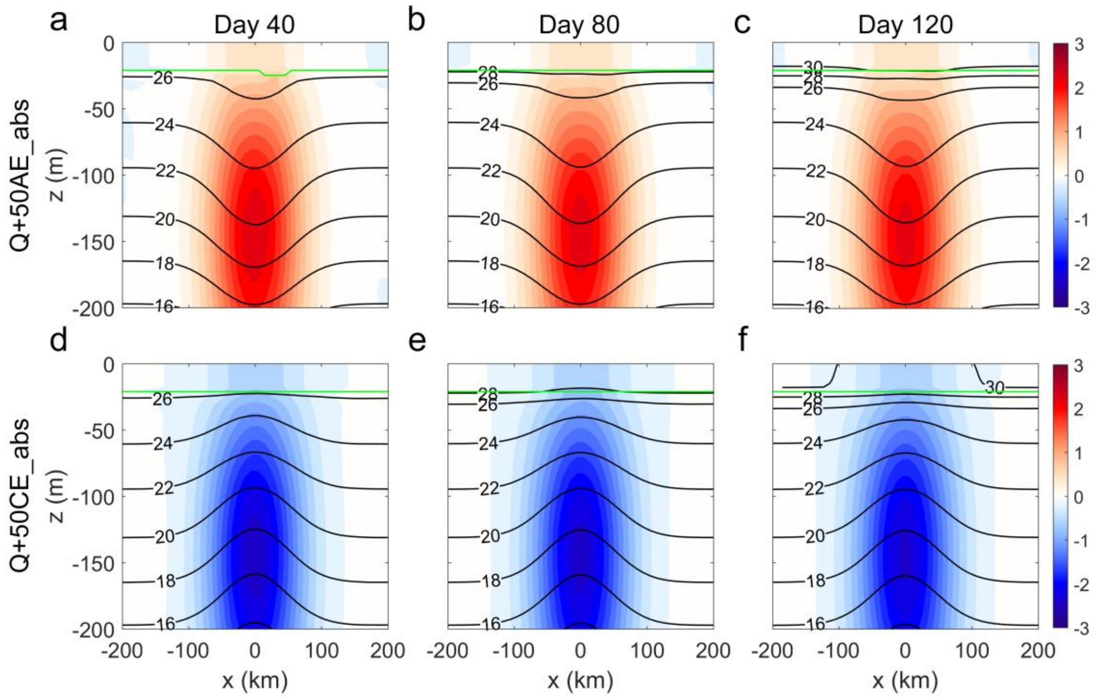

FIG. 9. (a-c) and (d-f) As Figs. 5a-c and Figs. 6a-c, but for the absolute wind stress experiments.

Next, we vary surface heat flux in the relative wind stress experiments to investigate the impact of surface mixed layer depth on the seasonal formation of CAEs and WCEs. Experiments Q+20AE_rel and Q+20CE_rel are the same as Q+50AE_rel and Q+50CE_rel, except that the surface heat flux is reduced from 50 W m^{-2} to 20 W m^{-2}. Due to the decrease in surface heating, the surface mixed layer becomes deeper (~30 m) and the stratification at the base of the mixed layer is weaker in Q+20AE_rel and Q+20CE_rel (Figs. 5d-f and 6d-f). It takes longer time for Ekman pumping induced by relative wind stress to develop negative (positive) anomalies at the base of the mixed layer in AE (CE) that are of comparable magnitude as those in Q+50AE_rel and Q+50CE_rel. As a result, although the initial positive (negative) SSTA at the center of the AE (CE) decreases (increases) to close to zero on day 120, the sign of eddy SSTA is not reversed (Figs. 7f and 8f).

In experiments Q-50AE_rel and Q-50CE_rel, we use a negative surface heat flux of -50 W m^{-2} to simulate the evolution of eddies under relative wind stress in winter. Under the combined influence of wind stress-induced mixing and surface cooling-induced convection, the mixed layer in these two experiments deepens significantly to about 90 m on day 120 (Figs. 5g-i and 6g-i). Although the overall eddy temperature anomalies are weakened in Q-50AE_rel and Q-50CE_rel as in the other four relative wind stress experiments, there are no reversing the sign of temperature anomalies at the base of the mixed layer and only slight weakening of SSTA at the center of the eddies by day 120 (Figs. 7g-i and 8g-i). Comparison of relative wind stress experiments forced with different surface heat fluxes highlights the importance of the depth of the surface mixed layer in regulating the seasonal cycle of the formation of CAEs and WCEs. Our results also imply that there is likely a lower chance of observing CAEs and WCEs in regions where the mixed layer is relatively deep all year round.

Figure 10 shows the temporal evolution of SSTA at the centers of the AE and CE in all the relative wind stress experiments. It is evident that the more positive the surface heat flux is, the shorter time it takes for the AE and CE to change sign of their SSTA, that is, evolving into a CAE and WCE. Furthermore, with the same surface heat flux forcing, it takes longer time for the CE to evolve into a WCE than for the AE to evolve into a CAE. For example, the time it takes for SSTA of the AE and CE to change sign in experiments Q+50AE_rel and Q+50CE_rel are 65 days and 88 days, respectively. A similar difference is also found between the AE and CE in experiments Q+20AE_rel and Q+20CE_rel. This result is consistent with the observations where the proportion of CAE is found to be systematically higher than that of WCE in the tropical oceans (Fig. 2). We explain this AE/CE asymmetry as follows. Although temperature anomalies change sign near the base of the mixed layer in both AE and CE experiments in response to Ekman pumping, the negative temperature anomalies in the AE experiments are centered at a shallower depth (close to or at the base of the mixed layer) than the positive temperature anomalies in the CE experiments due to the fact that relative wind stress induces Ekman upwelling in AE and downwelling in CE. Consequently, waters with larger temperature anomalies are entrained and mixed with the surface water by vertical mixing in the case of AE which reduces the time it takes to reverse the sign of initial eddy SSTA.

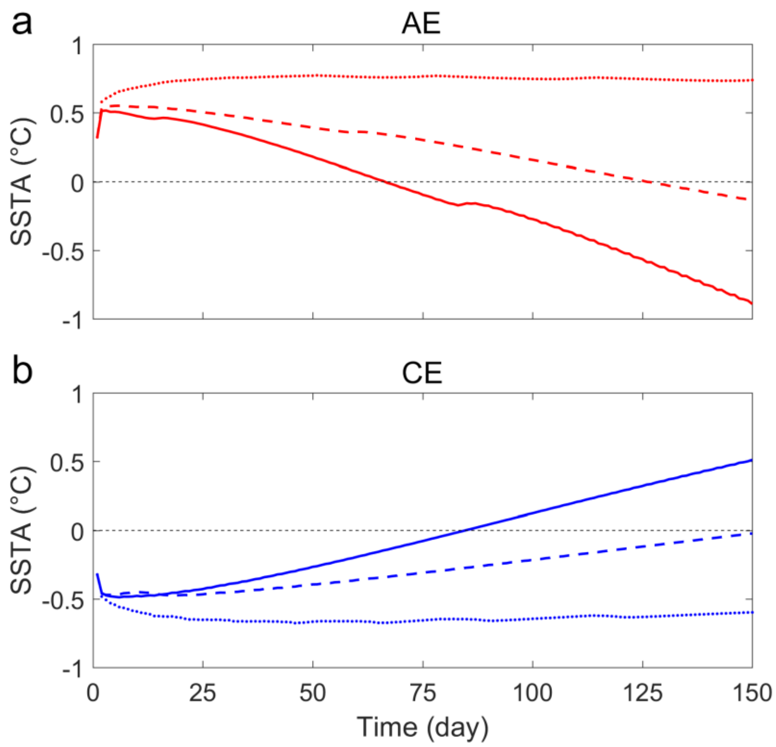

FIG. 10. Temporal evolution of SSTA (°C) at the centers of the simulated (a) AE and (b) CE with the relative wind stress. The solid, dashed and dotted curves represent results from experiments with surface heat flux of 50, 20 and -50 W m^{-2}, respectively.

5.2 Heat budget

To further verify the role of relative wind stress-induced Ekman pumping and turbulent mixing in the formation of CAEs and WCEs, we diagnose contributions of individual term in the heat budget equation for the AE and CE in experiments Q+50AE_rel and Q+50CE_rel over a 60-day period from day 60 to day 120, respectively:

$$\underbrace{\frac{\partial T}{\partial t}}_{Tendency} = -\underbrace{(u\frac{\partial T}{\partial x} + v\frac{\partial T}{\partial y}}_{Adv_h} + \underbrace{w\frac{\partial T}{\partial z}}_{Adv_z}) + \underbrace{K_h\left(\frac{\partial^2 T}{\partial x^2} + \frac{\partial^2 T}{\partial y^2}\right)}_{Diff_h} + \underbrace{K_z\frac{\partial^2 T}{\partial z^2}}_{Diff_z},$$

where K_h and K_z are the horizontal and vertical eddy diffusivities, respectively, Adv_h and Adv_z are the horizontal and vertical advection terms, and $Diff_h$ and $Diff_z$ are the horizontal and vertical diffusion terms. Note that the $Diff_z$ term at the surface is surface heat flux.

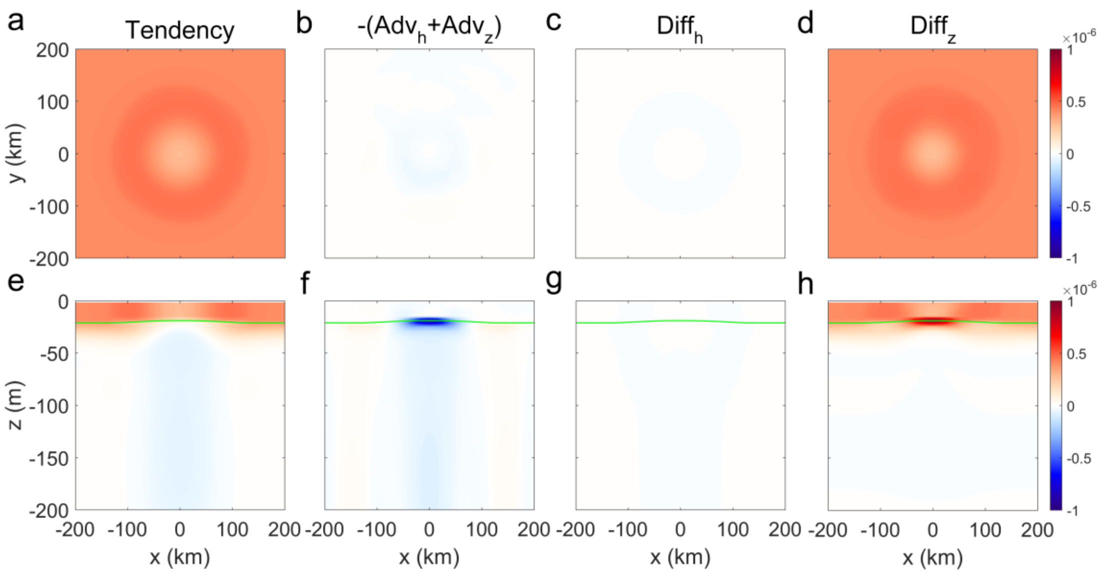

FIG. 11. Spatial patterns of individual term (°C s^{-1}) in the temperature equation averaged between day 60 and day 120 of the AE experiment (Q+50AE_rel). (a-d) At the depth of 15 m and (e-h) across y = 0. Green curves indicate the mean MLDs during this 60-day period.

Our analysis shows that the heat budget is almost closed for both experiments (Figs. 11 and 12) and the residuals are at least one order of magnitude smaller than the dominate terms. As we can see from the tendency terms, the AE and CE are in the process of evolving into a CAE and WCE, respectively, during this 60-day period. Below the mixed layer, there is a cooling tendency in AE and a warming tendency in CE (Figs. 11e and 12e). Both tendencies can be explained by the advection term (Figs. 11f and 12f) — the relative wind stress-induced Ekman pumping flattens the isotherms and weakens the initial temperature anomalies of the eddy. The maximum cooling and warming effect due to the advection term is located at the base of the mixing layer where the Ekman pumping velocity is large and the water is strongly stratified. Within the mixed layer, the overall tendency is for the water to become warmer (Figs. 11e and

12e) and this is due to surface heating which is included in the diffusion term in our diagnostics (Figs. 11h and 12h). However, this warming tendency is not spatially uniform. Owing to the large negative temperature anomalies developed at the base of the mixed layer of the AE as a result of Ekman upwelling, the water that is entrained upwards into the mixed layer by vertical mixing inside the AE is colder than that outside of the AE, which results in a minimum warming hole in the surface temperature of the AE (Figs. 11a and d) and hence the formation of the CAE. A similar process takes place in the mixed layer of the CE experiment which results in the formation of the WCE (Fig. 12). The horizontal diffusion term is small in both experiments and can be neglected in the heat budget. Our heat budget analysis confirms the important role of relative wind stress-induced Ekman pumping and vertical mixing in the generation of CAEs and WCEs.

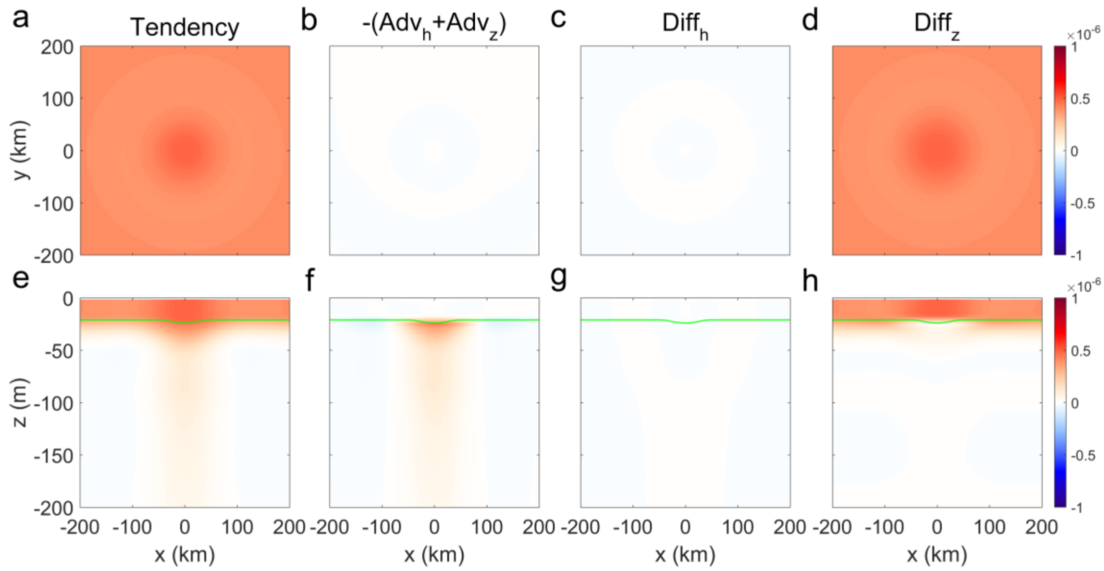

FIG. 12. As Fig. 11 but for the CE experiment (Q+50CE_rel).

6. Discussion and conclusion

Based on 20 years of satellite observations, we have shown that the probabilities of CAEs and WCEs are relatively high in the tropical oceans. Moreover, these unconventional eddies are found to occur more frequently in summer than in winter. Using composite eddy structures derived from Argo profiles in the tropical regions as initial conditions, we have conducted a suite of idealized numerical model experiments to investigate the mechanism behind the formation and seasonal cycle of CAEs and WCEs. It is found that when the surface mixed layer is shallow such as that at low latitudes in summer, Ekman pumping induced by relative wind stress is able to reverse the sign of eddy temperature anomalies at the base of the mixed layer. For example, negative temperature anomalies develop at the base of the mixed layer of an AE experiment (Q+50AE_rel) and positive temperature anomalies at the base of a CE experiment (Q+50CE_rel). Because of this, water that is entrained into the mixed layer from its base by vertical mixing is colder (warmer) inside the AE (CE) than that outside of it, which leads to negative (positive) eddy SSTA compared to the surroundings. In this way, the AE (CE) evolves into a CAE (WCE) under relative wind stress. When the mixing layer is deep such as that in winter or at high latitudes, it is difficult for relative wind Ekman pumping to reverse the sign of eddy temperature anomalies at the base of the mixed layer and as such the eddy SSTA does not reverse its sign as is found in Q-50AE_rel and Q-50CE_rel. The heat budget analysis and additional experiments with absolute wind stress further confirm the important role of relative wind stress-induced Ekman pumping and vertical mixing in the formation of CAEs and WCEs.

CAEs and WCEs have been found to be abundant in the global ocean and they modulate air-sea exchanges in a way that is different from their conventional counterparts (Leyba et al. 2017; Liu et al. 2020; Ni et al. 2021). Understanding how CAE and WCE are generated is a necessary first step if we are to understand their dynamics and properly represent their effects in the ocean climate models. Although our idealized modelling approach allows us to highlight and diagnose the important role of relative wind stress, surface mixed layer depth and vertical mixing in the generation of CAEs and WCEs, other processes in the open ocean, such as temporal or spatial wind stress and heat flux variability, eddy-atmosphere thermodynamic coupling, eddy-eddy interaction and background flow instability, may also influence the generation of these unconventional eddies but are not considered in this study. Furthermore, the mechanism for generating CAEs and WCEs near the boundary currents are thought to be different (e.g., Chaigneau et al. 2011; Itoh and Yasuda 2010; Sun et al. 2022). This recentlydiscovered abundance of CAEs and WCEs in the global ocean calls on further research on this topic.

Acknowledgments. Q. Ni is supported by the National Natural Science Foundation of China (42106011) and an International Postdoctoral Exchange Fellowship awarded by the Office of China Postdoctoral Council. X. Zhai is supported by a Royal Society International Exchanges Award (IEC/NSFC/170007). Z. Yang is supported by National Natural Science Foundation of China (41776006, 41822601) and Taishan Scholar Funds (tsqn201909052). D. Chen is supported by the National Natural Science Foundation of China (41730535).

Data Availability Statement. All the observational data used in this study are publicly available. The altimeter SLA data are available at http://marine.copernicus.eu/. The microwave SST data are available at http://www.remss.com/. The QuikSCAT wind speed data are available at https://cersat.ifremer.fr/. The Argo profile data are available at http://www.argo.org.cn/.

APPENDIX

To further investigate how the AE and CE respond to relative and absolute wind stress forcing, we plot the eddy density structures and vertical velocities in our numerical experiments. As expected, the initial density surfaces are depressed inside the AE while they are raised inside the CE (Figs. A1a and b). In the relative wind stress experiments, wind-eddy interaction leads to Ekman upwelling inside the AE and downwelling inside the CE, which acts to raise the density surfaces in AE and depress the density surfaces in CE (Figs. A1c-h). The spatial pattern and magnitude of vertical velocity in the positive surface heat flux experiments are comparable (Figs. A1c-f). The magnitude of vertical velocity in the surface mixed layer of the two surface heat loss experiments is significantly enhanced (Figs. A1g-h) due to interaction with cooling-induced convection. In contrast, in the absolute wind stress experiments where Ekman pumping due to wind-eddy interaction is absent, vertical motions inside the eddies are very weak (Figs. A1i-j). As a result, the density surfaces remain almost unchanged from their initial condition, except that the stratification at the base of the mixed layer becomes stronger due to positive surface heat flux. This analysis again confirms the importance of relative wind stress and the vertical motions inside the eddies it induces in the generation of CAEs and WCEs.

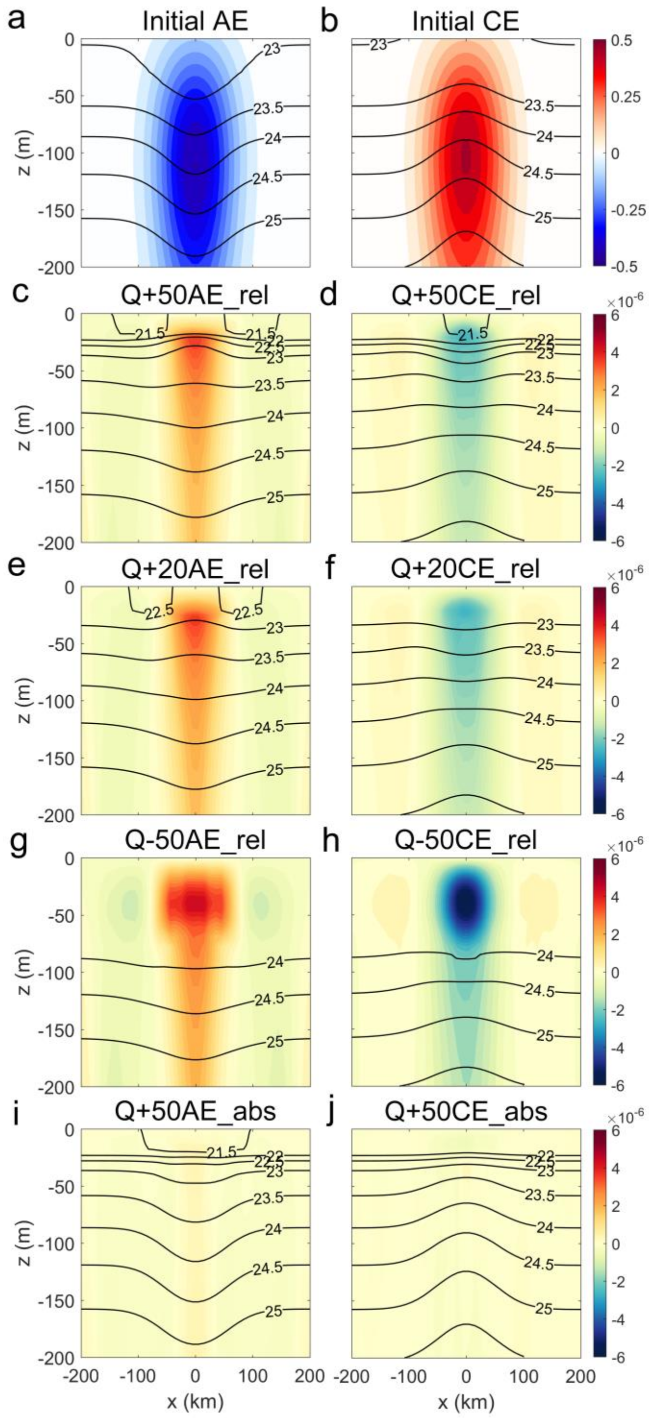

FIG. A1. (a, b) Initial eddy potential density (contours; kg m^{-3}) and potential density anomaly (colors; kg m^{-3}) fields at y = 0. (c-j) Vertical velocities (colors; m s^{-1}) at y = 0 averaged between day 60 and day 120 and potential density (contours; kg m^{-3}) at y = 0 on day 120 in all eight experiments.

REFERENCES

Assassi, C., and Coauthors, 2016: An index to distinguish surface- and subsurface-intensified vortices from surface observations. *J. Phys. Oceanogr.*, **46**, 2529-2552.

Chaigneau, A., M. L. Texier, G. Eldin, C. Grados, and O. Pizarro, 2011: Vertical structure of mesoscale eddies in the eastern South Pacific Ocean: A composite analysis from altimetry and Argo profiling floats. *J. Geophys. Res.*, **116**, C11025.

Chelton, D. B., M. G. Schlax, and R. M. Samelson, 2011: Global observations of nonlinear mesoscale eddies. *Prog. Oceanogr.*, **91**, 167-216.

Chelton, D. B., M. G. Schlax, R. M. Samelson, and R. A. de Szoeke, 2007: Global observations of large oceanic eddies. *Geophys. Res. Lett.*, **34**, L15606.

Conway, T. M., J. B. Palter, and G. F. de Souza, 2018: Gulf Stream rings as a source of iron to the North Atlantic subtropical gyre. *Nature Geosci.*, **11**, 594-598.

de Boyer Montégut, C., G. Madec, A. S. Fischer, A. Lazar, and D. Iudicone, 2004: Mixed layer depth over the global ocean: An examination of profile data and a profile-based climatology. *J. Geophys. Res.*, **109**, C12003.

Everett, J. D., M. E. Baird, P. R. Oke, and I. M. Suthers, 2012: An avenue of eddies: Quantifying the biophysical properties of mesoscale eddies in the Tasman Sea. *Geophys. Res. Lett.*, **39,** L16608.

Frenger, I., N. Gruber, R. Knutti, and M. Münnich, 2013: Imprint of Southern Ocean eddies on winds, clouds and rainfall. *Nature Geosci.*, **6**, 608-612.

Gaube, P., D. B. Chelton, R. M. Samelson, M. G. Schlax, and L. W. O'Neill, 2015:

Satellite observations of mesoscale eddy-induced Ekman pumping. *J. Phys. Oceanogr.*, **45**, 104-132.

Hausmann, U., and A. Czaja, 2012: The observed signature of mesoscale eddies in sea surface temperature and the associated heat transport. *Deep-Sea Res. II*, **70**, 60-72.

He, Q., H. Zhan, and S. Cai, 2020: Anticyclonic eddies enhance the winter barrier layer and surface cooling in the Bay of Bengal. *J. Geophys. Res.*, **125**, e2020JC016524.

Itoh, S., and I. Yasuda, 2010: Water mass structure of warm and cold anticyclonic eddies in the western boundary region of the subarctic north pacific. *J. Phys. Oceanogr.,* **40**, 2624-2642.

Large, W. G., J. C. McWilliams, and S. C. Doney, 1994: Oceanic vertical mixing: A review and a model with a nonlocal boundary layer parameterization. *Rev. Geophys.*, **32**, 363-403.

Leyba, I. M., M. Saraceno, and S. A. Solman, 2017: Air-sea heat fluxes associated to mesoscale eddies in the Southwestern Atlantic Ocean and their dependence on different regional conditions. *Clim. Dyn.*, 49, 2491-2501.

Liu, Y., L. Yu, and G. Chen, 2020: Characterization of sea surface temperature and air-sea heat flux anomalies associated with mesoscale eddies in the South China Sea. *J. Geophys. Res.*, **125**, e2019JC015470.

Liu, Y., Q. Zheng, and X. Li, 2021: Characteristics of global ocean abnormal mesoscale eddies derived from the fusion of sea surface height and temperature data by deep learning. *Geophys. Res. Lett.*, **48**, e2021GL094772.

Marshall, J., A. Adcroft, C. Hill, L. Perelman, and C. Heisey, 1997: A finite-volume, incompressible Navier-Stokes model for studies of the ocean on parallel computers. *J. Geophys. Res.*, **102**, 5753-5766.

McGillicuddy, D. J., 2015: Formation of intrathermocline lenses by eddy-wind interaction. *J. Phys. Oceanogr.*, **45**, 606-612.

Moschos, E., A. Barboni, and A. Stegner, 2022: Why do inverse eddy surface temperature anomalies emerge? The case of the Mediterranean Sea. *Remote Sens.* **14**, 3807.

Ni, Q., X. Zhai, G. Wang, and D. P. Marshall, 2020: Random movement of mesoscale eddies in the global ocean. *J. Phys. Oceanogr*., **50**, 2341-2357.

Ni, Q., X. Zhai, X. Jiang, and D. Chen, 2021: Abundant cold anticyclonic eddies and warm cyclonic eddies in the global ocean. *J. Phys. Oceanogr.*, **50**, 2793-2806.

Penven, P., V. Echevin, J. Pasapera, F. Colas, and J. Tam, 2005: Average circulation, seasonal cycle, and mesoscale dynamics of the Peru Current System: A modeling approach. *J. Geophys. Res.*, **110**, C10021.

Rai, S., M. Hecht, M. Maltrud, and H. Aluie, 2019: Scale of oceanic eddy killing by wind from global satellite observations. *Sci. Adv.*, **7**, eabf4920.

Roemmich, D. and J. Gilson, 2001: Eddy transport of heat and thermocline waters in the North Pacific: A key to interannual/decadal climate variability? *J. Phys. Oceanogr.*, **31**, 675-687.

Souza, J. M. A. C., C. de Boyer Montégut, C. Cabanes, and P. Klein, 2011: Estimation of the Agulhas ring impacts on meridional heat fluxes and transport using ARGO floats and satellite data. *Geophys. Res. Lett.*, **38**, 1-5.

Stammer, D., 1997: Global characteristics of ocean variability estimated from regional TOPEX/POSEIDON altimeter measurements. *J. Phys. Oceanogr.*, **27**, 1743-1769.

Sun, W., and Coauthors, 2022: Comparative analysis of four types of mesoscale eddies in the Kuroshio-Oyashio extension region. *Front. Mar. Sci.*, **9**, 984244.

Sun, W., C. Dong, W. Tan, and Y. He, 2019: Statistical characteristics of cyclonic warm-core eddies and anticyclonic cold-core eddies in the North Pacific based on remote sensing data. *Remote Sens.*, **11**, 208.

Wilder, T., X. Zhai, D. R. Munday, and M. Joshi, 2022: The response of a baroclinic anticyclonic eddy to relative wind stress forcing, *J. Phys. Oceanogr.*, **52**, 2129-2142.

Xu, C., X. Zhai, and X. Shang, 2016: Work done by atmospheric winds on mesoscale ocean eddies. *Geophys. Res. Lett.*, **43**, 12174-12180.

Zhai, X., H. L. Johnson, and D. P. Marshall, 2010: Significant sink of ocean-eddy energy near western boundaries. *Nature Geosci.*, **3**, 608-612.

Zhang, Z., W. Wang, and B. Qiu, 2014: Oceanic mass transport by mesoscale eddies. *Science*, **345**, 322-324.